Toyama Daigaku Kenkyusuisinkikou Suiso Doitai Kagaku Kenkyu Senta Kenkyu Hokoku
ISSN 2433-5908

Annual Report of Hydrogen Isotope Research Center,
Organization for Promotion of Research,
University of Toyama, JAPAN
VOL 37 2017

富山大学研究推進機構水素同位体科学研究センター

研　究　報　告

第 37 巻

2017

富山大学研究推進機構 水素同位体科学研究センター

HYDROGEN ISOTOPE RESEARCH CENTER,

ORGANIZATION FOR PROMOTION OF RESEARCH, UNIVERSITY OF TOYAMA

目　　次

論　文

C_3N_4 光触媒によるヨウ化水素水溶液からの水素生成	……	萩原英久 伊田進太郎 石原達己	…… 1
水素により制御可能な開閉器の実験的検証	……	赤丸悟士 村井美佳子 原　正憲	…… 11
室温近傍での真空蒸留に伴うトリチウム水の濃度変化	……	原　正憲 小林果夏 赤丸悟士 中山将人 庄司美樹 押見吉成 町田　修 安松拓洋	…… 19

ノート

種結晶法による CHA 型ゼオライトの繰り返し合成と構造変化	……	田口　明 中森拓実 米山優紀	…… 29

I N D E X

Original

H. HAGIWARA, S. IDA, T. ISHIHARA
Hydrogen Production on C_3N_4 Photocatalyst from Hydrogen Iodide Aqueous Solution ····· 1

S. AKAMARU, M. MURAI, M. HARA
Experimental study of a hydrogen-controllable switch of electric circuits ····· 11

M. HARA, K. KOBAYASHI, S. AKAMARU, M. NAKAYAMA, M. SHOJI,
Y. OSHIMI, O. MACHIDA, T. YASUMATSU
Changes in the concentration of tritiated water under vacuum distillation
at around ambient temperature ····· 19

Note

A. TAGUCHI, T. NAKAMORI, Y. YONEYAMA
Synthesis and Structural Change of CHA Type Zeolite
in the Repeated Seed-Growth Synthesis····· 29

富山大学研究推進機構水素同位体科学研究センター研究報告 37：1－9，2017.

論　文

C_3N_4 光触媒によるヨウ化水素水溶液からの水素生成

萩原　英久[1)]、伊田　進太郎[2)]、石原　達己[3,4)]

1) 富山大学 研究推進機構 水素同位体科学研究センター
〒930-8555　富山市五福 3190
2) 熊本大学大学院 先端科学研究部
〒860-8555　熊本市中央区黒髪 2-39-1
3) 九州大学 カーボンニュートラル・エネルギー国際研究所
〒819-0395　福岡市西区元岡 744
4) 九州大学大学院 工学研究院 応用化学部門
〒819-0395　福岡市西区元岡 744

Hydrogen Production on a C_3N_4 Photocatalyst from a Hydrogen Iodide Aqueous Solution

Hidehisa Hagiwara,[1)] Shintaro Ida,[2)] Tatsumi Ishihara[3,4)]

1) Hydrogen Isotope Research Center, Organization for Promotion of Research, University of Toyama, Gofuku 3190, Toyama, 930-8555, Japan
2) Faculty of Advanced Science and Technology, Kumamoto University Kurokami 2-39-1, Chuo-ku Kumamoto, 860-8555, Japan
3) International Institute for Carbon-Neutral Energy Research, Kyushu University Motooka 744, Nishi-ku, Fukuoka, 819-0395, Japan
4) Department of Applied Chemistry, Faculty of Engineering, Kyushu University Motooka 744, Nishi-ku, Fukuoka, 819-0395, Japan

(Received December 25, 2017; accepted June 22, 2018)

Abstract

Photocatalytic hydrogen production on graphitic carbon nitride (g-C_3N_4) from a hydrogen iodide (HI) aqueous solution was investigated with respect to light energy conversion. The photoabsorption and surface

area of g-C_3N_4 depended strongly on the preparation temperature. The highest photocatalytic activity for HI decomposition was obtained with g-C_3N_4 prepared at 773 K, which had high photoabsorption capacity. This study revealed that the activity for I_2 formation on the g-C_3N_4 surface could be improved to achieve efficient HI decomposition with stoichiometric H_2 and I_2 formation.

1. Introduction

Hydrogen is considered to be a clean next-generation energy carrier, as it can be produced from various sources and used to generate electrical or thermal energy without CO_2 emission. However, most commercial hydrogen gases are produced from fossil fuels by steam reforming with CO_2 emission [1]. Therefore, hydrogen is currently not a clean energy source. To overcome this situation, various methods of producing hydrogen by water decomposition using renewable energy sources have been studied [2]. Among these, the solar IS (iodine-sulfur) process is a relatively new hydrogen production method [3].

The IS process is a thermochemical water splitting cycle, and the solar IS process employs concentrated solar thermal energy as a heat source [4]. This process comprises three chemical reactions as shown below:

$$2HI \rightarrow H_2 + I_2\ (g) \qquad (723\ K) \qquad (1)$$

$$H_2SO_4\ (g) \rightarrow SO_2\ (g) + H_2O + 1/2O_2 \qquad (1123\ K) \qquad (2)$$

$$SO_2\ (g) + I_2 + 2H_2O \rightarrow 2HI + H_2SO_4\ (aq) \qquad (373\ K) \qquad (3)$$

The IS process results in complete thermal decomposition of water into H_2 and O_2 at high temperature. This process was expected to improve HI decomposition for practical use because the low HI decomposition ratio (ca. 20% at 673 K) limits its total efficiency.

To overcome this issue, photocatalytic HI decomposition was investigated in this study. If HI decomposition occurs on photocatalysts under UV or visible light, and sulfuric acid

decomposition is induced by infrared heating in sunlight, the conversion efficiency of the solar IS process would improve. While several studies have been published on photocatalytic HI decomposition [5,6], the photocatalytic activity of graphitic carbon nitride (g-C_3N_4) for HI decomposition has not yet been investigated. Graphitic carbon nitride is an organic semiconductor photocatalyst, which was reported in 2009, that shows activity for organic pollutants and water decomposition [7]. In this study, g-C_3N_4 was prepared from melamine at different temperatures, and the photocatalytic activity for HI decomposition was evaluated.

2. Experimental

2.1. Photocatalyst Preparation and Characterization

All reagents were used without further purification. The g-C_3N_4 photocatalysts were prepared by heating melamine (99.0%, Wako Pure Chemical Industries, Ltd., Japan) in air. The melamine powder (5 g) was placed in an alumina crucible and calcined at a predetermined temperature (723–973 K) in a muffle furnace. Platinum nanoparticles were employed as co-catalyst for the hydrogen evolution reaction. Pt was loaded on g-C_3N_4 using an evaporation to dryness method with aqueous tetraammineplatinum(II) nitrate ($Pt(NH_3)_4(NO_3)_2$, 99.995%, Sigma-Aldrich Co., USA). A mixture of C_3N_4 powder and Pt precursor was heated at 573 K for 2 h under hydrogen gas flow (50 ml min^{-1}).

X-ray diffraction (XRD) patterns of the samples were obtained with an X-ray diffractometer (RINT2000, Rigaku Corp., Japan) equipped with Cu Kα radiation. The Brunauer-Emmett-Teller (BET) surface area was determined with an adsorption apparatus (BELSORP-mini, MicrotracBEL Corp., Japan). UV–Vis and IR diffuse reflectance spectra were obtained with UV–Vis (UV-3600, Shimadzu Corp., Japan) and FT-IR (Nicolet 6700, Thermo Fisher Scientific Inc., USA) spectrophotometers, respectively. X-ray photoelectron spectroscopy (XPS) was performed with an X-ray photoelectron spectrometer (AXIS-165,

Shimadzu Corp., Japan).

2.2. Photocatalytic Reaction

Photocatalytic HI decomposition was performed in a quartz reactor containing 10 mM aqueous HI. The reactor was irradiated with a Xe lamp (2.0 W cm^{-2}) with magnetic stirring. The evolved gases were detected using a gas chromatograph (GC-8A, Shimadzu Corp., Japan) with a thermal conductivity detector. After the photocatalytic reaction, the catalyst was collected by centrifugation and separated from the reaction solution by decantation. The amounts of triiodide (I_3^-) and iodide (I^-) ions were determined by titration with aqueous $Na_2S_2O_3$ and $AgNO_3$, respectively.

3. Results and Discussion

Figure 1 shows XRD patterns of carbon nitrides prepared at different temperatures. Most of the diffraction peaks were assigned to g-C_3N_4, as reported previously [8]. While g-C_3N_4 was obtained above 773 K, the sample calcined at 973 K was completely decomposed. The

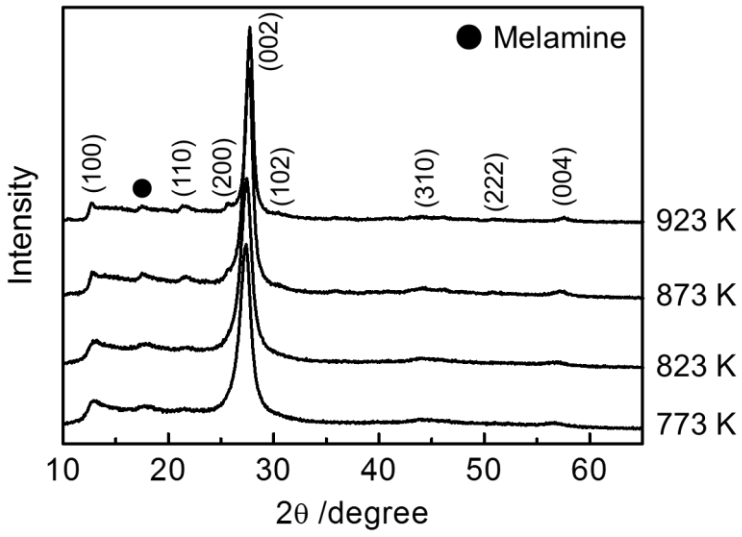

Fig. 1 XRD patterns of synthesized g-C_3N_4 powders.

Table 1 Weight change and specific surface area of samples calcined at different temperatures.

Calcination temp. /K	Weight of melamine /g	Weight of calcined sample /g	Specific surface area /m^2 g^{-1}
773	5.02	2.77	4.7
823	5.00	2.61	9.5
873	5.04	2.21	25.7
923	4.99	1.27	39.9

diffraction peaks of g-C_3N_4 became sharper as the calcination temperature increased, indicating that the crystallinity of g-C_3N_4 increased with the calcination temperature.

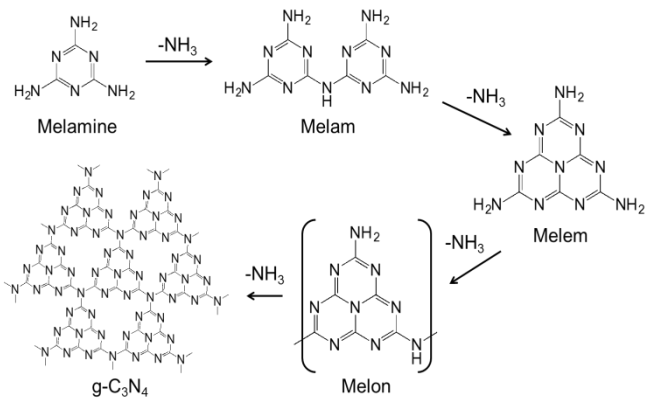

Fig. 2 Formation mechanism of g-C_3N_4 in thermal decomposition of melamine [9].

Table 1 shows the weight of the samples before and after calcination at each temperature. The weight loss during heat treatment was caused by sublimation of melamine and desorption of ammonia, which are driven by both deamination and the formation of aromatic units [9], as shown in Fig. 2. These reactions accelerate as the temperature increases. Therefore, melamine polymerization increased with the calcination temperature, and the weight of the prepared sample decreased due to deammoniation. These results were consistent with the XRD results. The specific surface area of the g-C_3N_4 samples, obtained by nitrogen gas adsorption, is also summarized in Table 1. The surface area increased with the calcination temperature, and that of a sample calcined at 923 K was about 40 m^2 g^{-1}. Furthermore,hysteresis loops were observed in the adsorption-desorption isotherms of all samples, which were identified as IUPAC type H3 [10]. It was thus confirmed that the carbon nitrides prepared in this study were agglomerates of plate-like crystals such as graphite.

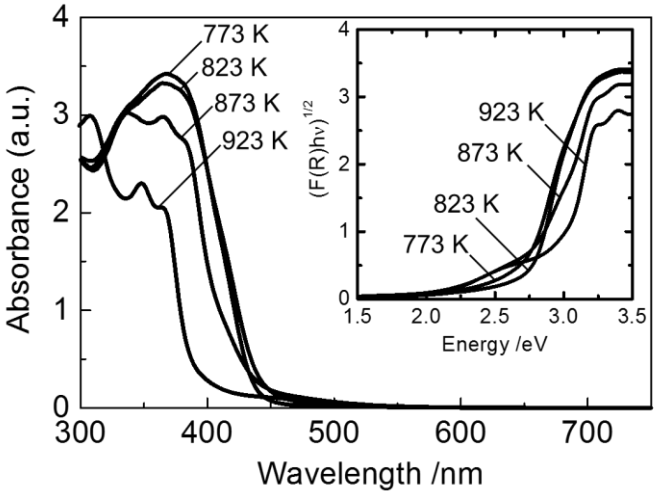

Fig. 3 UV–Vis DR spectra of g-C_3N_4 samples.

Figure 3 shows UV–Vis diffuse reflectance spectra of the prepared g-C_3N_4 samples. The absorption edge was 450 nm for the g-C_3N_4 calcined at 773 K, and this shifted to a shorter wavelength after heating at a higher temperature. The band gap energy of the samples can be determined from a plot of $(F(R)h\nu)^{1/2}$ versus light energy (Fig. 3 inset), where R, h, and ν are the reflectance coefficient, Planck's constant, and the light frequency. The optical band gaps of g-C_3N_4 calcined at 773, 823, 873, and 923 K were estimated as 2.7, 2.75, 2.8, and 3.0 eV, respectively. As the prepared g-C_3N_4 samples can absorb visible light, they are more favorable for solar energy conversion than TiO_2 photocatalysts.

Photocatalytic decomposition of HI on Pt/g-C_3N_4 was performed under Xe lamp irradiation. The control experiments showed that no detectable product was formed in the absence of either the photocatalysts or light irradiation. The main products of the photocatalytic HI decomposition were H_2 and I_3^-, which was produced by reaction between I_2 and I^-. As shown in Fig. 4, the photocatalytic activity of the g-C_3N_4 depended on the calcination

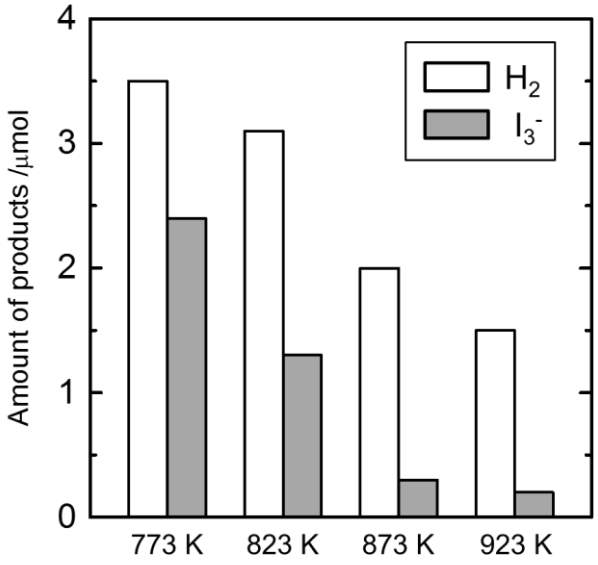

Fig. 4 Amounts of H_2 and I_3^- formed on Pt/g-C_3N_4 photocatalysts after HI decomposition for 12 h.

temperature. The g-C_3N_4 sample calcined at 773 K showed the highest hydrogen production during photocatalytic HI decomposition. This can be explained by differences in the light absorbed by the prepared g-C_3N_4 photocatalysts. However, the amounts of I_2 formed were below the stoichiometric amounts in all cases. To determine the reason for non-stoichiometric H_2 and I_2 (I_3^-) formation, XPS was performed. Figure 5 shows XPS spectra of the catalyst before and after photocatalytic HI decomposition with NaI as a reference. Despite washing several times with pure water, I 3d peaks were observed from the Pt/g-C_3N_4 catalyst after the reaction. This indicates the presence of strongly adsorbed iodine on the g-C_3N_4. Liu et al. reported that products accumulated on a g-C_3N_4 photocatalyst and inhibited photocatalytic reactions [11]. For HI photodecomposition on Pt/g-C_3N_4, no co-catalyst was used for I_2 formation, while a Pt co-catalyst was used for H_2 formation. Therefore, it appeared that I_2 formation on the g-C_3N_4 catalyst surface proceeded less easily than H_2 formation. Since the surface areas of the g-C_3N_4 catalysts prepared at a high calcination temperature tended to be large, it is believed that inhibition of the photocatalytic reaction also increased, due to iodine accumulation. Consequently, it is considered that g-C_3N_4 calcined at 773 K with a high photoabsorption capacity and a small surface area showed the highest photocatalytic activity for HI decomposition.

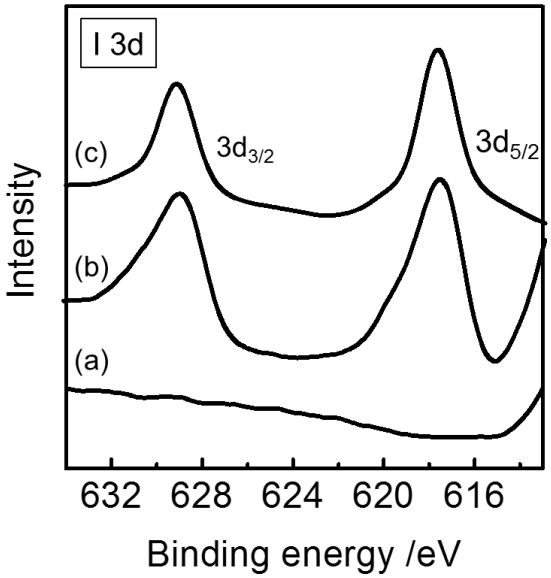

Fig. 5 XPS spectra of Pt/g-C_3N_4 prepared at 773 K (a) before and (b) after HI decomposition. (c) NaI reference data.

4. Conclusions

Photocatalytic hydrogen production on Pt/g-C_3N_4 from aqueous HI was investigated in this study. XRD, UV–Vis absorption spectra, and BET surface area measurements revealed that the crystallinity, photoabsorption properties, and surface area of the prepared g-C_3N_4 strongly depended on the calcination temperature. The highest photocatalytic activity for HI decomposition was obtained with g-C_3N_4 prepared at 773 K, due to its high photoabsorption capacity. Compared to H_2 formation, the activity of the Pt/g-C_3N_4 surface for I_2 formation appeared low; thus, co-catalysts should be employed for I_2 formation to improve the photocatalytic activity of g-C_3N_4 for HI decomposition.

Acknowledgement

This research was partially supported by JSPS KAKENHI Grant-in-Aid for Specially Promoted Research (JP16H06293), and Grant-in-Aid for Young Scientists (JP24686107). The authors would like to thank Enago (www.enago.jp) for the English language review.

References

[1] R. M. Navarro, M. A. Peña, J. L. G. Fierro, Chem. Rev. 107 (2007) 3952−3991.
[2] J. A. Turner, Science, 305 (2004) 972-974.
[3] C. Huang, A.T-Raissi, Solar Energy, 78 (2005) 632-646.
[4] D. O'keefe, C. Allen, G, Besenbruch, L. Brown, J. Norman, R. Sharp, Int. J. Hydrogen Energy, **7** (1982) 381.
[5] Y. I. Kim, S. Salim, M. J. Huq, T. E. Mallouk, J. Am. Chem. Soc., 113 (1991) 9561-9563.
[6] T. Ohno, S. Saito, K. Fujihara, M. Matsumura, Bull. Chem. Soc. Jpn., 69 (1996) 3059-3064.
[7] X. Wang, K. Maeda, A. Thomas, K. Takanabe, G. Xin, J. M. Carlsson, K. Domen, M. Antonietti, Nature Materials, 8 (2009) 76-80.
[8] M. J. Bojdys, J.-O. Müller, M. Antonietti, A. Thomas, Chem. Eur. J. 14 (2008) 8177–8182.
[9] Y. Wang, X. Wang, M. Antonietti, Angew. Chem. Int. Ed. 51 (2012) 68–89.
[10] K. S. W. Sing, D. H. Everett, R. A. W. Haul, L. Moscou, R. A. Pierotti, J. Rouquerol, T. Siemieniewska, Pure Appl. Chem. 57, (1985) 603-619.

[11] J. Liu, Y. Liu, N. Liu, Y. Han, X. Zhang, H. Huang, Y. Lifshitz, S.-T. Lee, J. Zhong, Z. Kang, Science, 347 (2015) 970-974.

富山大学研究推進機構水素同位体科学研究センター研究報告 37：11－18，2017.

論　文

水素により制御可能な開閉器の実験的検証

赤丸 悟士，村井 美佳子，原 正憲

富山大学研究推進機構水素同位体科学研究センター
〒930-8555　富山市五福 3190

Experimental study of a hydrogen-controllable switch of electric circuits

Satoshi Akamaru, Mikako Murai, Masanori Hara

Hydrogen Isotope Research Center, Organization for Promotion of Research, University of Toyama
Gofuku 3190, Toyama 930-8555, Japan

(Received January 12, 2018; accepted June 22, 2018)

Abstract

In this paper, the hydrogen-controllable switch of electric circuits was proposed. The concept of the switch is based upon hydrogen gas pressure controlling the switch condition, either opened or closed, without any electrical supports. The switch has been designed so that it is closed in an atmosphere that does sot contain hydrogen. To study its switching behaviors, the switch was placed in the argon gas flow. When flowing gas was changed to a gas mixture containing 9% H_2 – 91%Ar, the switch was open after 201 s. However, when the mixture was replaced by argon gas, the switch was closed again. In addition, we determined that the threshold for hydrogen concentration while turning the switch on could be adjusted by an arranging a magnet in the switch.

1. Introduction

Safe handling of hydrogen (H_2) gas is a critical issue in the supply network of large

amounts of H_2 gas. The H_2 gas is flammable in air at concentration levels of 4-75%, which is a wider range compared to methane and gasoline [1]. Therefore H_2 concentration levels must be monitored at all times in order to maintain safety levels while handling the H_2 gas. In general, if the H_2 concentration in the atmosphere reaches above 1%, all ignition sources must be removed as soon as possible. One of the main ignition sources are electric circuits. As the ignition energy for a mixture of air and hydrogen is relatively low, a small electric spark can ignite the mixture [1]. Thus all electrical equipment in the work space must be turned off when a H_2 leak is detected.

Almost all safety devices operating in the hydrogen-containing air atmosphere require electrical supply, and the safety device can also ignite the mixture. Therefore safety devices without an electrical supply are favorable to maintain safety while H_2 handling. A unique switching device, namely, a magnetic switch controlled by hydrogen gas, is described in this paper. A typical magnetic switch is operated by the change in the external magnetic field. The magnetic field is generated from either an electrical current or a permanent magnet. The switch described in this paper can be controlled by not magnetic field but by H_2 gas within a certain pressure. The switch does not require electrical supply to control it; only H_2 gas can control the switch. Consequently, this switch provides a safe mechanism for using in hydrogenous environment.

In this paper, we explain the basic mechanisms of the hydrogen-controllable switch of electric circuits, how the test switch was constructed, and the methods in which the characteristics of the switch relative to H_2 gas were verified.

2. Experimental

2.1. Principle of operation of the hydrogen-controllable switch

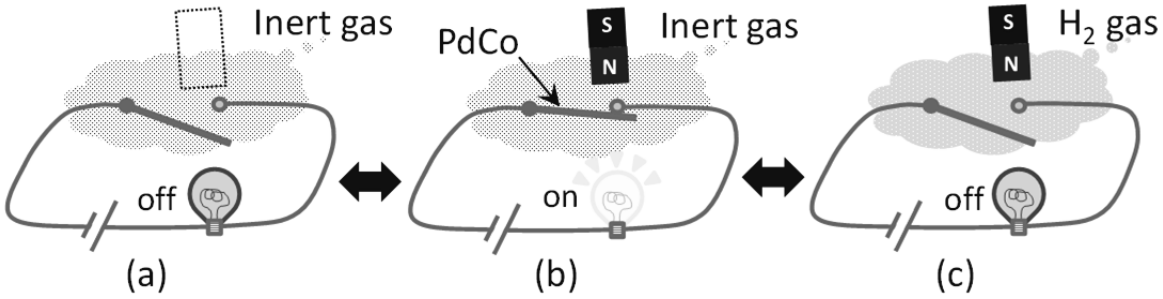

Fig. 1. Basic mechanisms of the hydrogen-controllable switch.

The basic mechanisms of the hydrogen-controllable switch are depicted in Fig. 1. The plate in the switch contains ferromagnetic hydrogen absorbing alloy PdCo. The plate is movable, and the permanent magnet can control both opening and closing of the electrical circuit. Initially, without the permanent magnet the plate is set to open the switch (Fig. 1a). The permanent magnet is placed near the PdCo-containing plate, and the plate contacts a terminal, turning thus the switch on (Fig. 1b).

When hydrogen appears in the surrounding atmosphere, PdCo absorbs hydrogen and the magnetization of PdCo is reduced [2]. As the results, attractive force between the magnet and the PdCo-containing plate is reduced, and the plate leaves from the terminal turning thus the switch off (Fig. 1c).

If hydrogen gas leaves the surrounding atmosphere, PdCo desorbs hydrogen, and the PdCo-containing plate contacts the terminal again. This switch can be used repeatedly, and thus works as the hydrogen-controllable switch.

2.2. Experimental test of operation of the hydrogen-controllable switch

The schematic view of the experimental system is illustrated in Fig. 2. The switch was assembled from two Cu rods, a 0.01 mm thick Cu plate with the $Pd_{0.9}Co_{0.1}$ alloy powder deposited on the back side, an NdFeB magnet, and a glass cell. The opposite sections of each

copper rod were machined in such a way that they were flat surface facing each other across a small gap. The Cu plate (with $Pd_{0.9}Co_{0.1}$ alloy on the back side) was put on one flat surface and was bound with Cu wire. A terminal of the plate was bent into a triangular shape, perpendicular to the upper Cu rod. The apparatus described above was covered by the glass cell, and the NdFeB magnet was placed outside of the cell. The position of the NdFeB magnet was adjusted so that the Cu plate touched the upper Cu rod.

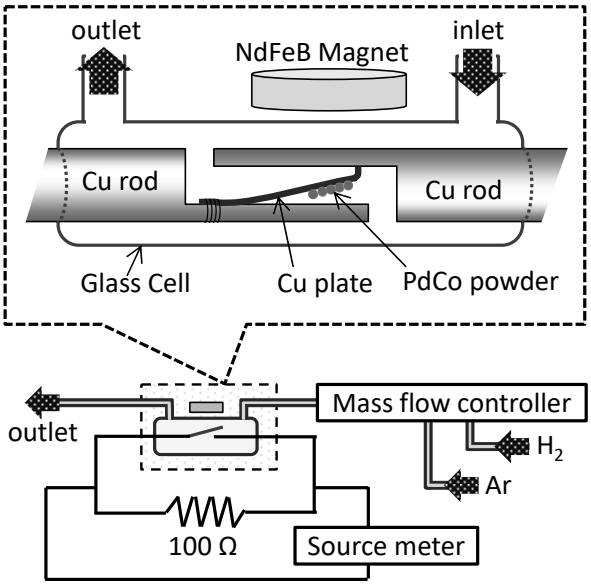

Fig. 2. Schematic view of the basic components to show switching behaviors.

The switch was connected to the low voltage SourceMeter instrument, Keithley 2401. A 100 Ω resistor was set parallel to the switch. The direct electrical current of 100 mA, supported by the SourceMeter instruments, flowed constantly through an electrical circuit, and the changes in the voltage were continuously monitored as measurements were performed. H_2 and Ar gases were supplied to each mass flow controller, making a mixture with a certain H_2 concentration. The mixture flowed into the cell with flow rate of 100 ml/min.

3. Results and discussion

Figure 3 illustrates the typical experimental result for the hydrogen-controllable switch. The distance between the cell and the magnet $d_{\text{sw-mag}}$ was 0.7 cm. The voltage E_{all} showed almost 0 V under Ar gas flow at time t less than 0 second, indicating that the switch was

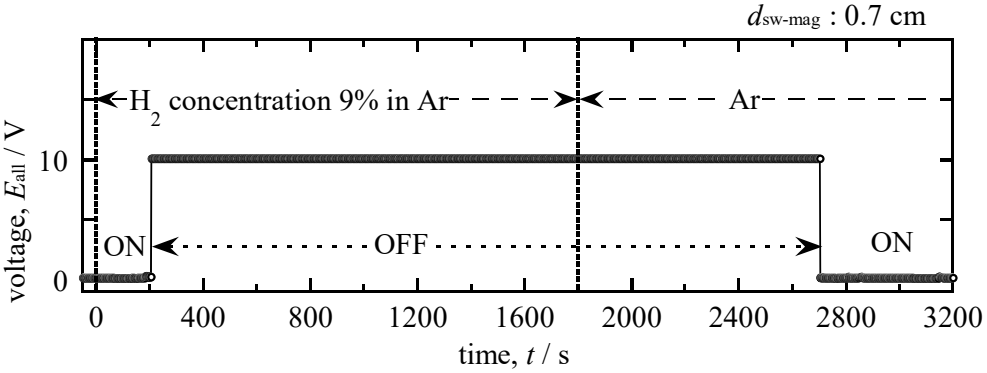

Fig. 3. Typical switching behavior of the hydrogen-controllable switch. H_2 was added to Ar at t = 0 s, and H_2 addition to Ar was stopped at 1800 seconds. The H_2 concentration in the H_2-Ar mixture and the distance between the cell and the magnet were fixed at 9% and 0.7 cm, correspondingly.

closed, namely, the Cu plate maintained contact with the upper Cu rod. The gas that flowed into the cell was changed at t = 0 s to the mixture of H_2 and Ar with H_2 concentration of 9%. At t = 206 s, the E_{all} quickly changed to 10 V, indicating that the switch was turned off, namely, the Cu plate was no longer in contact with the upper Cu rod. The switch was held open during the H_2-Ar mixture flow. The flowing gas in the cell was changed to Ar at t = 1800 s. After 904 seconds from the change of the flowing gas (corresponding to t = 2704 s), the E_{all} became almost 0 V again. Changing the E_{all} to 0 V implied that the switch was turned on, namely, the Cu plate made contact with the upper Cu rod. These results indicate that the switch, constructed in this study, is controlled by using a mixture of 9% H_2 in Ar.

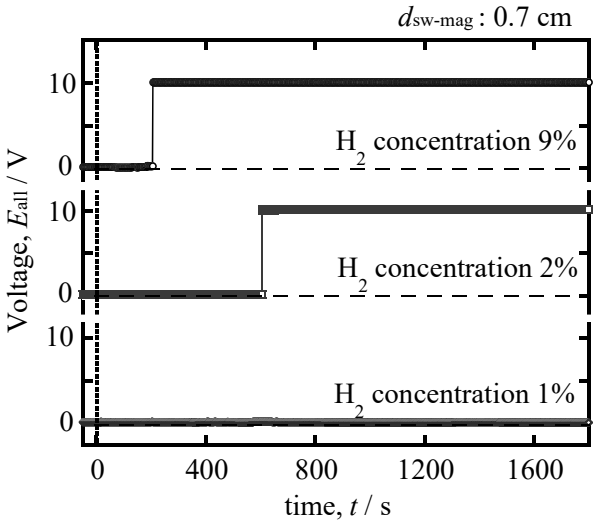

Fig. 4. Switching behavior for various H_2 concentration in the H_2-Ar gas mixture. The distance between the cell and the magnet was 0.7 cm.

Figure 4 illustrates the switching

behavior with different H_2 concentrations in the H_2-Ar gas mixture. The experimental conditions, except H_2 concentration, were the same as in Fig. 3. With H_2 concentrations of 9% and 2%, the switch was turned off at t = 206 s and 606 s, respectively. However, the switch remained closed at the H_2 concentration of 1% in the H_2-Ar gas mixture. It appeared that there was the threshold of H_2 concentration to turn the switch off. In addition, the time to turn the switch off at the H_2 concentration of 2% was three times longer than at the H_2 concentration of 9%. These facts can be explained by the following reasons. The switch was turned off when the attractive force between the magnet and the PdCo alloy was smaller than the gravity and/or the elastic force of the Cu plate. The attractive force is generally governed by a magnetization of the PdCo alloy and the distance between the switch and the magnet. Note that the magnetization of PdCo becomes smaller as higher H_2 partial pressure [2], and the magnetization is proportional to the square root of H_2 partial pressure [3]. In this experimental condition, the magnetization of the PdCo alloy under the H_2 concentration of 1% was larger than threshold magnetization M_{th}. This is the value required to keep equilibrium between the magnetization-induced attractive force on the one hand, and teh gravity and the elastic force of the Cu plate on the other hand. The rate of hydrogen absorption is higher at higher H_2 partial pressure, so the magnetization of the PdCo alloy reaches M_{th} faster under higher H_2 partial pressure.

Figure 5 shows the switching behavior with a slightly longer distance between the cell and the magnet, $d_{sw\text{-}mag}$, which was set to 0.9 cm. The switch was turned off with the

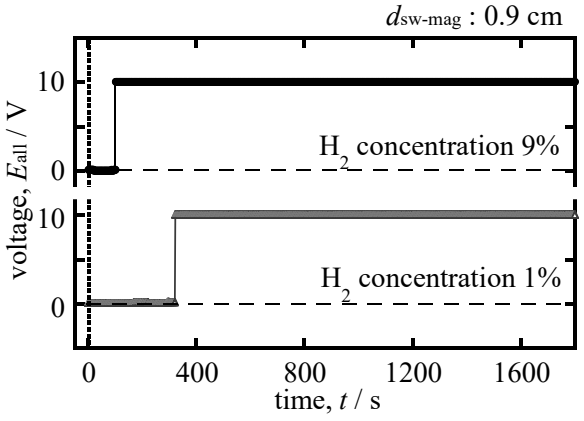

Fig. 5. Switching behavior after changing the distance between the cell and the magnet to 0.9 cm.

H_2 concentration of 9% at t = 101 s. This time was shorter than for $d_{sw\text{-}mag}$ = 0.7 cm. At the H_2 concentration of 1%, the switch was turned off at t = 322 s. These results demonstrate qualitatively that the attractive force between the magnet and the PdCo alloy becomes weaker with longer distance $d_{sw\text{-}mag}$. Consequently, it indicated that the threshold of the H_2 concentration to turn the switch off could be adjusted by the distance between the magnet and the PdCo alloy.

A significant problem emerged from this experiment is an instability of the electric contact between the Cu plate and the upper Cu rod. We observed that E_{all} did not change to almost 0 V whereas the Cu plate seemed to be attached to the upper plate. There are two reasons for this instability. The first reason is a weakness of the attractive force without H_2 gas, and the other reason was the surface condition at the contact point. The former reason can be solved by the development of a high performance ferromagnetic hydrogen absorbing alloy, which is favorable in demonstrating a large change of magnetization by hydrogen absorption. The solution for the latter reason is coating the plate with less oxidation materials such as Pt, it is possible to improve the contact. In future we will try to improve the switch.

4. Conclusions

The hydrogen-controllable switch was demonstrated through an experiment. The switch was similar to a conventional reed switch but was characterized using ferromagnetic hydrogen absorbing alloy PdCo with one side of contact. The switch was generally closed by using the permanent magnet taking advantage of the attractive force between the magnet and the PdCo alloy. The switch spontaneously opened in the presence of hydrogen gas due to a decrease in magnetization of the PdCo alloy occurring in the presence of hydrogen gas. While the basic behaviors mentioned above have been confirmed, some improvements are necessary in order to obtain a stable hydrogen-controllable switch.

Acknowledgement

This study was supported by the future technology research fund, University of Toyama.

References

[1] H. Fayaz, R. Saidur, N. Razali, F. S. Anuar, A. R. Saleman, M. R. Islam, *Renewable and Sustainable Energy Reviews* **16** (2012) 5511-5528.

[2] S. Akamaru, T. Matsumoto, M. Hara, K. Nishimura, N. Nunomura, M. Matsuyama, *Journal of Alloys and Compounds* **580** (2013) S102-S104.

[3] N. Nunomura, M. Hara, S. Akamaru, *Proceedings in PRICM8: Pacific Rim International Congress on Advanced Materials and Processing* (2013) 1837-1841.

富山大学研究推進機構水素同位体科学研究センター研究報告 37：19－28，2017.

論文

室温近傍での真空蒸留に伴うトリチウム水の濃度変化

原　正憲[1]，小林　果夏[1]，赤丸　悟士[1]，中山　将人[1]，庄司　美樹[2]，
押見　吉成[3]，町田　修[3]，安松　拓洋[3]

1 富山大学　研究推進機構　水素同位体科学研究センター
〒930-8555　富山市五福 3190
2 富山大学　研究推進機構　アイソトープ実験施設
〒930-0194　富山市杉谷 2630
3 東京パワーテクノロジー株式会社　福島原子力事業所
〒979-1305　福島県双葉郡大熊町大字熊字錦台 182-1

Changes in the concentration of tritiated water under vacuum distillation at around ambient temperature

Masanori Hara[1], Kana Kobayashi[1], Satoshi Akamaru[1], Masato Nakayama[1], Miki Shoji[2], Yoshinari Oshimi[3], Osamu Machida[3], Takuyo Yasumatsu[3]

1 Hydrogen Isotope Research Center, Organization for Research Promotion, University of Toyama
Gofuku 3190, Toyama city, Toyama 930-8555, JAPAN
2 Life Science Research Center, Organization for Research Promotion, University of Toyama
Sugitani 2630, Toyama city, Toyama 930-0194, JAPAN
3 Fukushima Nuclear Power Branch, Tokyo Power Technology Ltd
Nishikidai 182-1 kuma, Okuma-machi, Futaba-gun, Fukushima 979-1305, JAPAN

(Received December 13, 2017；accepted June 22, 2018)

Abstract

When measuring the tritium concentration in environmental water by liquid scintillation counting, distillation of the water sample is indispensable. To investigate changes the tritium concentration during distillation, tritiated water was distilled under vacuum at around ambient temperature. During vacuum distillation, the tritium concentration in the residual sample water increased and that in the condensed sample water decreased. The change in the tritium concentration during the distillation process was explained by Rayleigh distillation model. When the volume of the condensed water sample was about 80 % of that of the original sample, its tritium concentration was about 97 % of that in the original sample. Therefore, water sample should be distilled above 80 % of sample water to keep an underestimation of tritium concentration within 3 %.

１．緒言

トリチウムは測定が困難な放射性同位元素のひとつである。これは，トリチウムの放射壊変により発生するβ線の最大エネルギーは 18.6 keV と小さいためである。通常，液体中のトリチウムは液体シンチレーション計測法[1]により測定される。この計測法では，液体の測定試料を液体シンチレータと直接混合し，液体シンチレーションカウンタでの計測用試料とする。計測用試料内でトリチウムの放射壊変が起こりβ線が発生すると，β線の運動エネルギーが液体シンチレータに移行し，発光が誘起される。この発光を液体シンチレーションカウンタに装備されている光電子増倍管により検出する。つまり，シンチレーション発光の頻度がトリチウムの放射壊変の頻度に対応し，液体試料中のトリチウムを定量できる。しかし，液体シンチレーション計測法での測定には，いくつかの問題点がある。液体の測定試料中に共存する化学種が，シンチレーション発光を起こす分子へのβ線のエネルギーの移行を妨げる。この現象はクエンチング（消光作用）と呼ばれる。クエンチングはシンチレータの発光効率を低下させ，シンチレーション発光の検出効率を低下させる。また，有色の試料ではシンチレーション過程により生成した光子を吸収するカラークエンチングが起こり検出効率を低下させる。これらクエンチングの影響を緩和させるために，測定試料に対して蒸留処理を行うことがある[2]。特に，海水，鉱水中の極低濃度のトリチウムを検出する場合には，蒸留による処理が必要である[2，3]。

トリチウムは１つの陽子と２つの中性子で原子核を構成する水素同位体であり，原子核

が１つの陽子で構成される軽水素に比べ３倍の質量数となる。このため，水素同位体の置換は物理化学的特性に大きな同位体効果を生じる。例えば，重水（D_2O）の融点は 276.97 K, 軽水（H_2O)では 273.15 K であり，その差は 3.78 K である。トリチウム水（T_2O）の融点は 277.64 K である[4]。融点は重い同位体に置換することにより高くなることが知られている。このため，トリチウム水（HTO）を含む試料水の一部を蒸留した際には，蒸留され捕集された水中のトリチウム濃度が減少することが考えられる。

液体シンチレーション測定用の試料調製中の蒸留処理によるトリチウム水の濃度の変化は，極低濃度トリチウム水中のトリチウム測定において極めて重要な問題である。蒸留操作によるトリチウム水の濃度変化を知るために，トリチウム水の真空蒸留を行い，液体シンチレーションカウンタによりトリチウム濃度を測定した。

２．実験

２．１　実験手順

一般的に同位体効果は低温で大きくなることから，低温で効率的に蒸留が進む真空蒸留法を用いた。図１に装置図を示す。装置はガラス製である。装置は蒸発側容器と凝縮側容器がバルブを介して接続されている。蒸発側容器を所定の蒸留温度とし，凝縮側を液体窒素温度に冷却することでトリチウム水の真空蒸留を行った。使用したトリチウム水は 8.4 kBq/ml の比放射能を持ち，一回の実験に約 2 ml 使用した。

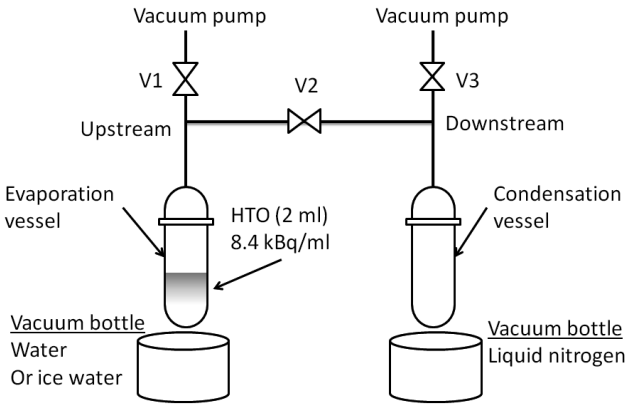

Fig. 1. Schematic diagram of vacuum distillation system for tritiated water.

実験手順の詳細なフローを図 2 に示す。最初に蒸発側容器，凝縮側容器の乾燥重量を測定した。蒸発側容器に 2.2 ml のトリチウム水を入れ，そこから 0.2 ml を分取した。分取したトリチウム水に 15 ml の液体シンチレータ（Ultima Gold LLT）を加え，測定用カクテルを調製した。カクテル中のトリチウムを液体シンチレーションカウンタで測定し，蒸留前の

トリチウム濃度 $R_{L,0}$ を決定した。液体シンチレーションカウンタにはLSC-LB5を使用した。分取後，トリチウム水を含む蒸発側容器の重量を測定し，蒸留に使用するトリチウム水の量 W_0 を求めた。重量測定後，蒸発側容器を装置に取り付けた。トリチウム水を液体窒素温度で氷とし，系内の空気を油回転ポンプにより排気した。トリチウム水中に溶解している気体を除去するために，トリチウム水をいったん融解させ，溶解していた気体を系内に放出させた。再び，トリチウム水を液体窒素で冷却し，系内の排気を行った。排気後，蒸発側のトリチウム水は水浴を用いて所定の蒸留温度とした。次いで，下流側の凝縮側容器を液体窒素で冷却した。冷却後，バルブ V2 を開き，真空蒸留を開始した。所定時間経過後，バルブ V2 を閉め蒸留を終了した。蒸留終了後，蒸発側容器と凝縮側容器の重量を計ることにより，残留トリチウム水量 W_L と蒸留トリチウム水量 W_V を求めた。計量後，蒸発側容器，凝縮側容器よりそれぞれ 0.2 ml のトリチウム水を分取し，液体シンチレータと混合し液体シンチレーションカウンタによりトリチウム濃度 R_L，R_V を定量した。ここで添え字の L は蒸発側容器を示し，V は凝縮側容器を示す。

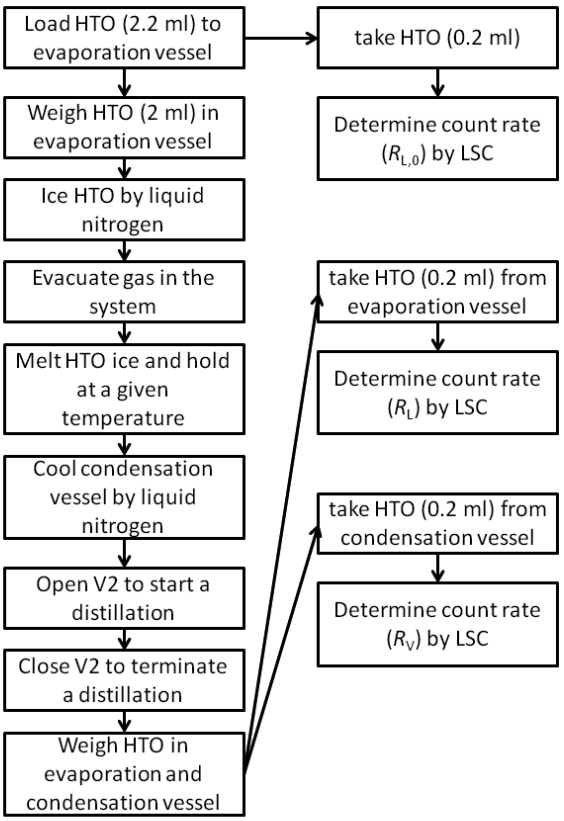

Fig. 2. Procedure of vacuum distillation for tritiated water.

２．２　蒸留によるトリチウム濃度変化の解析

蒸留中のトリチウム濃度の変化の解析には，レイリーの単蒸留モデルを適用した[5]。ここでは軽い成分（H_2O）と重い成分（HTO)の混合液の蒸留を考える。このモデルでは，蒸発した成分は，液相に戻ることはなく，系から取り除かれるとする。

蒸留開始後のある時間 t で蒸発側容器中に存在する混合液の全量を N_L とする。その中の H_2O 成分と HTO 成分のモル分率を mH_2O_L，$mHTO_L$ とする。ここで，添え字の L は液相（蒸発側容器）を表す。HTO の存在比は

$$R = \frac{mHTO_L}{mH_2O_L} \qquad (1)$$

となる。また，

$$mH_2O_L = \frac{1}{1+R} \quad (2)$$

$$mHTO_L = \frac{R}{1+R} \quad (3)$$

で表される。

時間$(t+\Delta t)$の経過とともに蒸留が進み，ΔN_V だけ蒸気となり液相から取り除かれ，液相内のモル分率が，ΔmH_2O_L，$\Delta mHTO_L$ だけ変化する。この時の気相中のモル分率の変化は

$$\Delta mH_2O_V = -\Delta mH_2O_L \qquad (3)$$

$$\Delta mHTO_V = -\Delta mHTO_L \qquad (4)$$

で表される。ここで，添え字の V は気相（凝縮側容器）を表す。時間 Δt の前後での物質のやり取りは

$$N_L \cdot mHTO_L = (N_L - \Delta N_V)(mHTO_L + \Delta mHTO_L) + \Delta N_V \cdot (mHTO_V + \Delta mHTO_V) \quad (5)$$

となる。左辺は時間 t の HTO の状態，右辺は時間 $t+\Delta t$ のときである。$\Delta N_V = -\Delta N_L$ なので

$$0 = N_L \cdot \Delta mHTO_L + \Delta N_L \cdot mHTO_L + \Delta N_L \cdot \Delta mHTO_L - \Delta N_L \cdot mHTO_V - \Delta N_L \cdot \Delta mHTO_V \quad (6)$$

となる。ここで，$\Delta N_L \cdot \Delta mHTO_L$ と $\Delta N_L \cdot \Delta mHTO_V$ は微小量どうしの積なので，$\Delta N_L \cdot \Delta mHTO_L \approx 0$ として，

$$N_L \cdot \Delta mHTO_L + \Delta N_L \cdot mHTO_L = \Delta N_L \cdot mHTO_V \qquad (7)$$

が得られる。同様に，H_2O に着目すれば

$$N_L \cdot \Delta mH_2O_L + \Delta N_L \cdot mH_2O_L = \Delta N_L \cdot mH_2O_V \qquad (8)$$

が得られる。式(7)，式(8)を整理して

$$\frac{mHTO_V}{mHTO_L} = \frac{N_L \cdot \Delta mHTO_L}{\Delta N_L \cdot mHTO_L} + 1 \qquad (9)$$

$$\frac{mH_2O_V}{mH_2O_L} = \frac{N_L \cdot \Delta mH_2O_L}{\Delta N_L \cdot mH_2O_L} + 1 \qquad (10)$$

が得られる。ここで，分別係数(fractionation factor, α)を導入し，

$$\alpha = \frac{\frac{mHTO_V}{mH_2O_V}}{\frac{mHTO_L}{mH_2O_L}} \qquad (11)$$

とする。式(11)に式(9)，式(10)を代入して

$$\alpha\left(\frac{\Delta mH_2O_L}{mH_2O_L}+\frac{\Delta N_L}{N_L}\right)=\left(\frac{\Delta mHTO_L}{mHTO_L}+\frac{\Delta N_L}{N_L}\right) \qquad (12)$$

となる。ここで，Δを時間の微分量にして，

$$\alpha\left(\frac{1}{mH_2O_L}\frac{dmH_2O_L}{dt}+\frac{1}{N_L}\frac{dN_L}{dt}\right)=\left(\frac{1}{mHTO_L}\frac{dmHTO_L}{dt}+\frac{1}{N_L}\frac{dN_L}{dt}\right) \qquad (13)$$

とあらわされ，これを積分し

$$\alpha\ln\frac{mH_2O_L}{mH_2O_{L,0}}=\ln\frac{mHTO_L}{mHTO_{L,0}}+(1-\alpha)\ln\frac{N_L}{N_{L,0}} \qquad (14)$$

となる。なお，添え字の 0 は蒸留前を示す。次に，液相（蒸発側容器）の残留割合とする f を導入する。

$$f=\frac{N_L}{N_{L,0}} \qquad (15)$$

存在比 R を用いて式(14)を整理すると

$$\alpha\ln\left(\frac{1+R_0}{1+R}\right)=\ln\left(\frac{1+R_0}{1+R}\frac{R}{R_0}\right)+(1-\alpha)\ln f \qquad (16)$$

とあらわされる。R_0 は蒸留前の存在比である。ここで，存在比 R は HTO と H_2O の比なので, HTO の濃度が十分に小さいことより , $1+R\approx1$ および $1+R_0\approx1$ と近似できる。よって，

$$(\alpha-1)\ln f=\ln\left(\frac{R}{R_0}\right) \qquad (17)$$

となる。f は液相の残留割合なので，蒸留の進行割合である進行度を p とすれば，

$$(\alpha-1)\ln(1-p)=\ln\left(\frac{R_L}{R_{L,0}}\right) \qquad (18)$$

$$(1-p)^{(\alpha-1)}=\frac{R_L}{R_{L,0}} \qquad (19)$$

となる。ここで，Rが示す相を明瞭とするため添え字を付した。一方，式(19)は液相（蒸発側容器）に着目しているので，気相（凝縮側容器）に着目すると式(18)は

$$(1-\alpha)\ln p = \ln\left(\frac{R_V}{R_{V,0}}\right) \qquad (20)$$

$$p^{(1-\alpha)} = \frac{R_V}{R_{V,0}} \qquad (21)$$

と表される。ここでαは軽い同位体に対する重い同位体の分別係数であるので，通常は 1 以下となる。なお，$R_{L,0} = R_{V,0}$である。

実験により得られた，もともとの試料水のトリチウム濃度に対する蒸留後のトリチウム水濃度の比は蒸発側が$\frac{R_L}{R_{L,0}}$，凝縮側が$\frac{R_V}{R_{V,0}}$に対応している。縦軸に蒸留前のトリチウム水と蒸留後のトリチウム水の濃度の比，横軸に蒸留の進行度としてグラフを作成し，式(19)，式(21)でフィッティングすることにより，分別係数を得ることができる。また，蒸留の温度依存性は分別係数(α)に現れる。

３．結果と考察

図３から５に 273 K，297 K，313 K でのトリチウム水の蒸留結果を示す。縦軸は初期のトリチウム水濃度に対する蒸留後のトリチウム水濃度の比を示し，式(19)，式(21)の右辺に対応する。横軸は蒸留の進行度を表し，実験当初のトリチウム水の重量と蒸留後のトリチウム水の重量比である W_V/W_0 で求めた。蒸留の進行度は式(19)，式(21)中の p に対応する。図中の白抜き印は凝縮側容器，黒塗り印は蒸発側容器のトリチウム水濃度の比を示す。再現性を確認するために室温（297 K）で 2 回の蒸留実験を行った（図 4 参照）。2 回の蒸留実験の結果は，蒸発側容器中と凝縮側容器中のトリチウム水の蒸留に伴う濃度比の変化は一致しており，再現性が確認された。

図３から５より，蒸留を行ったいずれの温度においても，蒸発側容器中のトリチウム水の濃度は蒸留の進行とともに大きくなった。一方，凝縮側容器中のトリチウム水の濃度は蒸留が進むにつれて，当初のトリチウム濃度に近づいた。この傾向は，蒸留温度が低いほど明瞭に表れ，273 K の蒸留では蒸発側容器中のトリチウム水濃度は試料水を 80 %蒸留した時点で当初のトリチウム水濃度の 1.2 倍程度まで濃縮され，凝縮側容器のトリチウム水の濃度は当初のトリチウム水濃度の 0.95 倍程度であった。

液体シンチレーションカウンタによる極低濃度トリチウム水の測定において，蒸留された後のトリチウム水を使用するため，測定試料中のトリチウム水の濃度は蒸留前に比べ減少する。このため，液体シンチレーションカウンタで評価される試料中のトリチウム濃度は過少に評価される。この影響を評価するために，蒸留中のトリチウム濃度比の変化をレイリーの単蒸留モデルを使用して解析を行った[5]。その結果は図 3 から 5 中の実線で示した。いずれの温度においても，蒸発側容器中，凝縮側容器中のトリチウム水の濃度比の変化はレイリーモデルにより再現できた。

液体シンチレーションカウンタでの測定試料調製に必要となる凝縮側容器中の

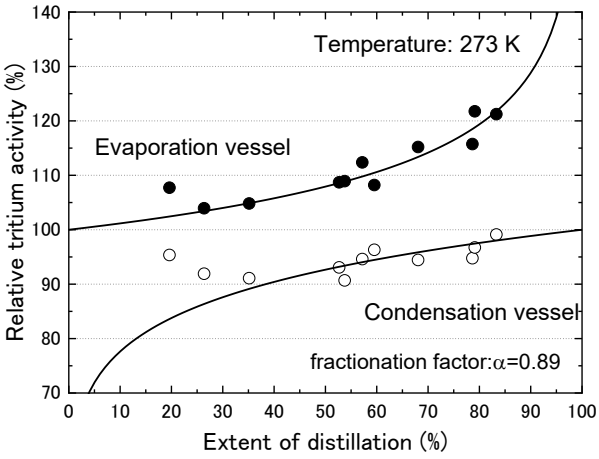

Fig. 3. Change in tritium activity during vacuum distillation at 273 K.

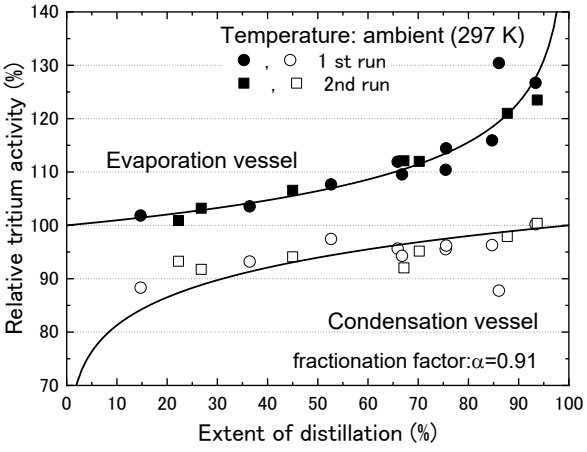

Fig. 4. Change in tritium activity during vacuum distillation at 297 K.

トリチウム水の濃度比の変化を得られた弁別係数を用いて求めた。その結果を図 6 に示す。蒸留操作でのトリチウム水の濃度低下を 2 %以下に抑えるためには，室温程度である 297 K では 80 %以上の試料水を蒸留する必要がある。実際，文部科学省により示されているトリチウム測定マニュアルでは，蒸留を試料が乾固する寸前まで行うと記載されている[2]。一方，図 4 に示したように蒸留操作におけるトリチウム水の濃縮挙動は再現性があるため，あらかじめ蒸留過程でのトリチウム水の濃度比の変化を測定しておけば，補正ができることが示唆される。

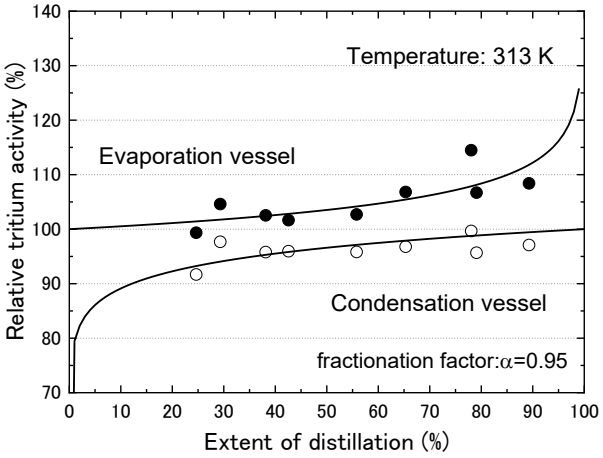

Fig. 5. Change in tritium activity during vacuum distillation at 313 K.

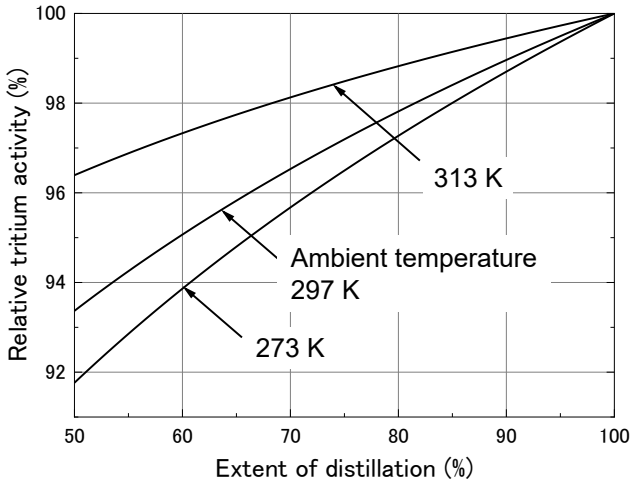

Fig. 6. Estimation of tritium activity in condensation vessel from Rayleigh distillation.

４．まとめ

水中の極低濃度のトリチウム水を液体シンチレーション測定法により定量する際には，電解濃縮等のトリチウム濃縮を行ったのちに試料水の蒸留が必要である。この蒸留を行うことにより，液体シンチレーション測定法で問題となるクエンチングの影響を軽減できるのみならず，液体シンチレータで保持できる試料水を多くすることができ，検出効率を向上させることができる。しかし，蒸留操作はトリチウム水の濃度を減少させる同位体効果を引き起こす。蒸留操作中のこの同位体効果の影響を室温近傍でトリチウム水を真空蒸留することにより評価した。

真空蒸留を進めるに従い，蒸発側容器ではトリチウム水の濃度は濃くなり，凝縮側容器で

はトリチウム水の濃度は当初のトリチウム水の濃度に近づいた。297 K において蒸留中のトリチウム水の濃度変化の再現性を確認した。蒸留中のトリチウム水の濃度変化はレイリーの単蒸留モデルで再現できた。

得られた結果より，液体シンチレーション計測法での試料調製に蒸留操作を適用する際には，できる限り全量に近い試料水を蒸留する必要があることが分かった。例えば，297 K 程度で蒸留を行う際，トリチウム濃度の減少を 2 %以下にするためには試料水の 80 %以上を蒸留する必要があることが分かった。一方，蒸留中のトリチウム水の濃度変化には再現性が見られたことから，実際の蒸留条件でトリチウム水の濃度変化をあらかじめ測定しておくことにより，蒸留操作によるトリチウム水の濃度の減少を補正できることが示唆された。

参考文献

[1] M. F. L'Annunziata and M. J. Kessler, "Liquid scintillation analysis: principles and practice", Chapt. 5, "Hand book of radioactivity analysis, 2nd ed", M. F. L'annunziata Ed., 2003, acadmic press.

[2] 文部科学省　科学技術・学術政策局　原子力安全課防災環境対策室編　”トリチウム分析法”,　放射能測定シリーズ 9，財団法人日本分析センター　2002

[3] G. T. Cook, C. J. Passo, Jr., B. Carter, "Environmental liquid scintillation analysis", Chapt. 6, "Hand book of radioactivity analysis, 2nd ed", M. F. L'annunziata Ed., 2003, acadmic press.

[4] M. Ceriotti, W. Fang, P. G. Kusalik, R. H. McKenzie, A. Michaelides, M. A. Morales, T. E. Markland, "Nuclear quantum effects in water and aqueous system: experiment, theory, and current challenges", Chem. Rev., 116(2016)7529-7550.

[5] 酒井　均，松久　幸敬，安定同位体地球化学，1996 年，東京大学出版会

富山大学研究推進機構水素同位体科学研究センター研究報告 37：29－38，2017.

ノート

種結晶法による CHA 型ゼオライトの繰り返し合成と構造変化

田口 明*，中森拓実，米山優紀

富山大学　研究推進機構　水素同位体科学研究センター

〒930-8555　富山市五福 3190

Synthesis and Structural Change of CHA Type Zeolite in the Repeated Seed-Growth Synthesis

Akira Taguchi*, Takumi Nakamaori, Yuki Yoneyama

Hydrogen Isotope Research Center

Organization for Promotion of Research, University of Toyama

Gofuku 3190, Toyama 930-8555

(Received January 19, 2018; accepted June 22, 2018)

Abstract

The synthesis of CHA type zeolite using seed crystals was studied. CHA zeolite could be obtained by seeded growth synthesis, where the initial seeds of CHA zeolite were prepared by the hydrothermal conversion of FAU zeolite. However, the subsequent use of the resultant CHA zeolite as seed crystals resulted in a structure change to sanidine and analcine.

Research note

Zeolites have applications in a variety of fields including detergent builders, adsorbents/desiccants and catalysts [1]. Recently, chabazite type zeolites, comprising 8-membered rings and assigned the framework type CHA by the International Zeolite Association [2], have been attracting new attention. This is because high silica CHA zeolite (so-called SSZ-13) or silicoaluminophosphate (SAPO-34) catalyzes the methanol-to-olefin reaction with high olefin (ethylene and propylene) selectivity [3-5]. More recent studies have shown that CHA zeolite, especially, copper-ion exchanged SSZ-13 (Cu-SSZ-13), provides a high NOx reduction activity using NH_3 as a reductant (NH_3-SCR) [6-8].

There are two main methods for the synthesis of CHA zeolite. One is a widely known, reliable method with potential applicability to the synthesis of SSZ-13, which uses N,N,N-trimethyladamantammonium hydroxide as an organic structure directing agent (OSDA) [5,9-11]. The other is the structure conversion method, where a well-defined zeolite is hydrothermally converted to CHA zeolite. Using FAU type zeolite as the starting material is probably the most popular method for CHA synthesis [12]. We also prepared CHA zeolite (K^+-type) from FAU (H-Y) zeolite, and found an intrinsic H_2 and D_2 sorption properties in subsequently Na^+ or Ca^{2+} ion-exchanged CHA zeolites [13].

One drawback of this CHA zeolite synthesis, especially for SSZ-13, is the use of expensive OSDA. This underscores the importance of developing CHA zeolite synthesis without requiring OSDA. Using seed crystals of CHA zeolite in zeolite growth is a progressive process, and Imai et al. successfully achieved seed-assisted CHA zeolite growth [14]. Also, Liu et al. reported the ultrafast (within 10 min) synthesis of CHA zeolite by using a continuous-flow reactor [15]. However, the initial seed crystals of CHA used in their experiments were prepared using OSDA. In the present report, we studied the seed-assisted growth of CHA zeolite, where the initial CHA zeolite was prepared by structure conversion method from FAU

zeolite.

Potassium type CHA zeolite was prepared by the hydrothermal conversion of FAU zeolite as described in the literature [9,10]. To 16.1 mL of a KOH (45 wt%) aqueous solution, 15 g of HY-zeolite (HSZ-320HOA, Tosoh Corp.) was added. Then, 119 mL of deionized water was poured, followed by vigorous shaking for 30 sec. The mixed solution was kept static in an oven at 100 ºC for 4 days. After cooling to room temperature, the precipitate was recovered by filtration, washed with water, and dried overnight at 100 ºC. The white solid was calcined at 600 ºC for 3 h under air flow (ca. 100 cm^3/min), with a ramp rate of 2 ºC/min. The obtained sample was denoted as CHA-HT. Figure 1 (a) shows the XRD (X-ray diffraction) patterns of CHA-HT. The diffraction signals were assignable to those from the CHA structure [2], suggesting the successful preparation of CHA zeolite.

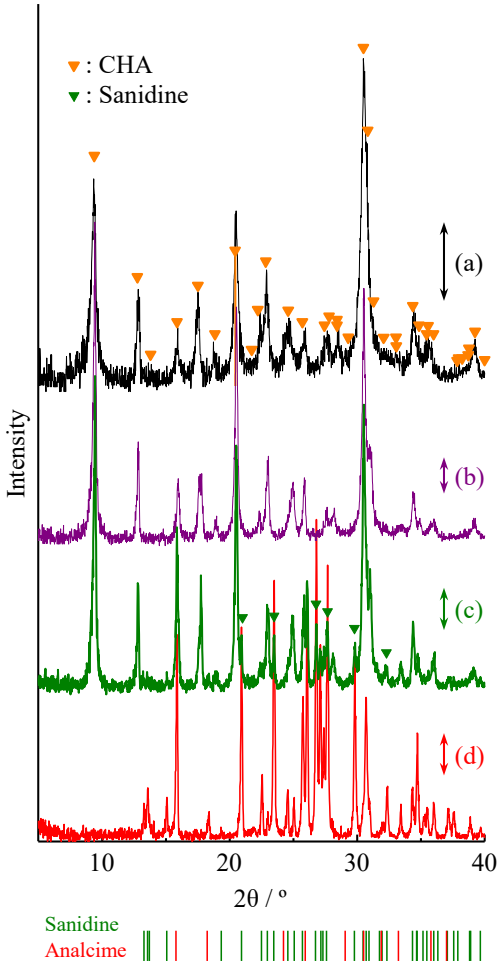

Fig. 1 XRD patterns of (a) CHA-HT, (b) CHA-Seed1, (c) CHA-Seed2 and (d) CHA-Seed3. The lengths of the arrows beside (a) to (d) each correspond to 100 cps. The expected positions of signals from sanidine and analcime are schematically drawn at the bottom.

Using CHA-HT as seed crystals, the growth of CHA zeolite with an amorphous aluminosilicate gel under hydrothermal conditions was investigated. Here, the mixed solution of fumed silica (1.0 g, Cab-O-Sil (M-5); Cabot Corporation, USA), $NaAlO_2$ (0.13 g), NaOH (0.47 g), KOH (0.17 g; all from Wako Pure Chemical Industries, Ltd.) in H_2O (30 mL) was used for preparing synthetic aluminosilicate gel according to the literature [14]. The molar

Table 1　Preparation and Si/Al ratio estimated by EDS and ^{29}Si MAS NMR measurements

Sample name	Synthetic conditions	Yield /g	Si/Al ratio	
			EDS	NMR
CHA-HT	Hydrothermally synthesized	-	2.5	2.17
CHA-Seed1	Synthesized using CHA-HT as a seed	0.45	3.0	2.73
CHA-Seed2	Synthesized using CHA-Seed1 as a seed	0.47	3.4	2.76
CHA-Seed3	Synthesized using CHA-Seed2 as a seed	0.41	4.0	n.d.

composition of this synthetic aluminosilicate gel corresponded to 1.0 SiO_2 : 0.1 $NaAlO_2$: 0.7 NaOH : 0.18 KOH : 100 H_2O. To this synthetic solution, CHA-HT (20 wt%, corresponding to about 0.36 g) as the seed crystals was added, and the mixture was hydrothermally treated at 170 ºC for 24 h with tumbling at 20 rpm using a hydrothermal synthesis reactor instrument (HIRO COMPANY). The product, denoted as CHA-Seed1 (see Table 1 for a summary of sample names), was obtained by filtration, drying and calcination in the same manner as mentioned above. The yield of CHA-Seed1 was higher than the weight of the seed crystals used, indicating that crystal growth from the synthetic alminosilicate gel had occurred.

The XRD pattern of CHA-Seed1 was as shown in Figure 1 (b). The diffraction signals were assignable to those from the CHA structure. Also, the diffraction signals were sharper and considerably more intense as compared with CHA-HT, suggesting that the crystallinity of CHA zeolite had been improved. The crystalline morphology of CHA-Seed1 observed by FE-SEM (JEM-6701F, JEOL) is represented in Figure 2 (b), together with that of CHA-HT (Figure 2 (a)). CHA-HT was composed from an aggregation of cube shaped crystals, the size of which generally ranging from several ten to 100 nm. On the other hand, CHA-Seed1 comprised of a stack of slab shaped crystals. The size of slabs was not uniform, ranging from several ten to several hundred nm. These were significantly different from those of CHA-HT, and the large sizes of crystals were consistent with the intense diffraction signals from CHA-Seed1.

In this study, further growth of CHA zeolites was also studied. CHA-Seed2 was prepared from the synthetic aluminosilicate gel in the same manner as mentioned above. Here, 20 wt% of CHA-Seed1 was used as seed crystals (Table 1). Subsequently, the resulting CHA-Seed2

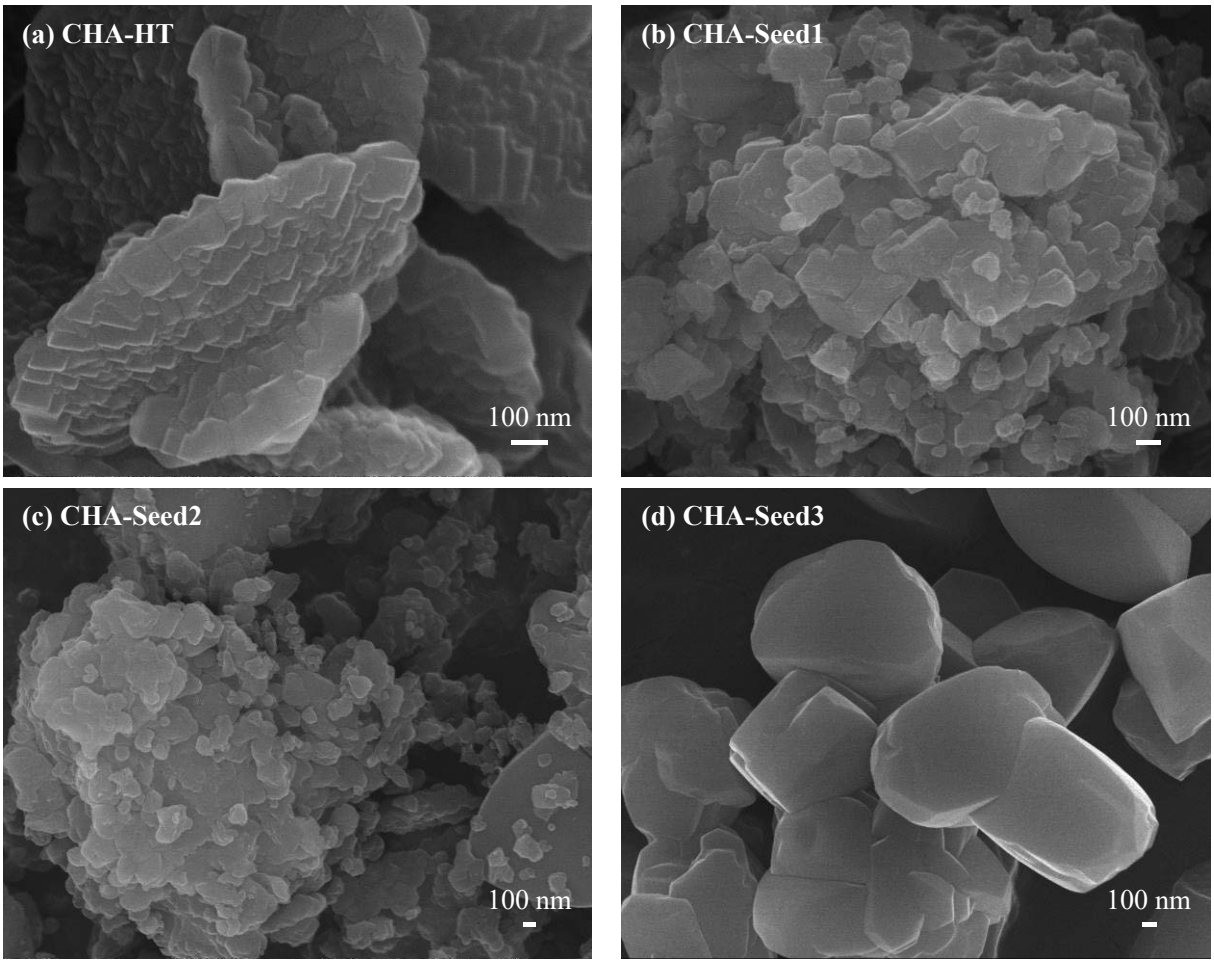

Fig. 2 FE-SEM pictures of (a) CHA-HT, (b) CHA-Seed1, (c) CHA-Seed2 and (d) CHA-Seed3.

was used as seed crystals for the preparation of CHA-Seed3. The XRD patterns of the obtained CHA-Seed2 and CHA-Seed3 were as shown in Figure 1. For the CHA-Seed2, although well-resolved and intense diffraction signals from the CHA structure could be confirmed, the diffraction signals assignable to sanidine (general formula; $(K,Na)(Si,Al)_4O_8$, JCPDS: 025-0618), for example, at 20.9, 23.5, 26.8, 27.7, 29.8 and 32.2º (2θ) were observed (marked signals in Figure 1 (c)). The latter signals, as well as other signals that appeared newly or had been hidden in the signals from CHA-Seed2, dominated in CHA-Seed3 (Figure 1 (d)). The diffraction signals were assignable to sanidine and analcime (ANA, general formula; $Na(Si_2Al)O_6 \cdot H_2O$, JCPDS: 041-1478) based on their peak positions illustrated in Figure 1. The drastic change of crystalline structure in CHA-Seed3 could be confirmed by FE-SEM study.

The crystalline morphology of CHA-Seed3, an aggregation of nonuniform ellipsoid-shaped crystals with the size of about several hundred to 1,000 nm, was totally different from that of CHA-HT or CHA-Seed1 (Figure 2). Thus, it was found that the seeded growth of CHA zeolite under hydrothermal conditions caused the collapse of specific CHA structures. Actually, the FE-SEM study of CHA-Seed2 showed large ellipsoid-shaped crystals rarely (e.g. on the right side in Figure 2 (c)), while the main product was slab shaped crystals.

The Si/Al ratio estimated by EDS (Energy-dispersive) spectroscopy (JEOL, JED-2300) combined with FE-SEM increased from 2.48 in CHA-HT to 2.97, 3.44 and 3.96 in CHA-Seed1, CHA-Seed2 and CHA-Seed3, respectively, showing an increase in Si content by the subsequence growth of CHA zeolite (Table 1). Imai et al. reported that the seed crystals mostly dissolved in this synthetic aliminosilicate gel in 1 h (170 ºC) [14]. Thus, the above results are consistent with the dissolution-recrystallization growth of CHA zeolite. Also, zeolites are not in a thermodynamically stable phase but in a metastable phase [16]. Therefore, the non-optimal synthetic conditions in this study is considered to have resulted in the formation of undesired aluminosilicates from CHA zeolite during repeated synthesis. It should be noted that the hydrothermal synthesis of aluminosilicate gel without seed crystals resulted in the formation of PHI type zeolite [2,14].

The growth and the structural change of CHA zeolite were investigated by using MAS (magic-angle spinning) NMR spectroscopy (at 6 kHz spinning, ECX-500, JEOL). Figure 3 shows the single-pulse spectra of ^{29}Si MAS NMR. Mainly, the resonance signals were observed at about -88, -92, -98, -103 and -108 ppm. These signals were assignable to Si(4Al), Si(3Al), Si(2Al), Si(1Al) and Si(0Al), respectively. Here, *n* in Si(*n*Al) indicates the number of Al atoms bonding to Si *via* O. One interesting point is that the relative intensities of Si(0Al) and Si(1Al) of CHA-Seed1 increased in comparison with those of CHA-HT. In addition, the

relative intensities of Si(3Al) and Si(4Al) decreased in CHA-Seed1. This suggests an increase in the number of Si-O-Si bonds in CHA zeolite made by seeded growth. CHA-Seed3, on the other hand, showed broadening of signals. As the XRD measurement revealed, CHA-Seed3 was a mixture of sanidine and analcime. Thus, the overlapping of Si(2Al) signals from two different aluminosilicates gave rise to the broadening of signals. Besides, sanidine is a polymorph crystal. This suggests that the heterogeneity of the Si tetrahedral environment led to the broadening of resonance signals.

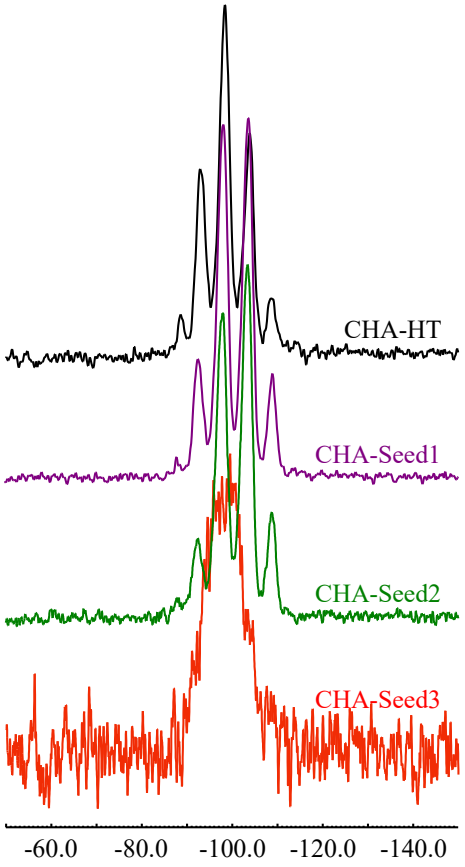

Fig. 3 ^{29}Si MAS NMR spectra of (a) CHA-HT, (b) CHA-Seed1, (c) CHA-Seed2 and (d) CHA-Seed3.

The framework Si/Al ratio can be determined from signal intensities using the following equation [17]:

$$(\mathrm{Si/Al}) = \sum_{n=0}^{4} A_{\mathrm{Si}\,(n\,\mathrm{Al})} \Big/ \sum_{n=0}^{4} \frac{n}{4} A_{\mathrm{Si}\,(n\,\mathrm{Al})}$$

Here, A is the signal area of Si(nAl). The Si/Al ratio was estimated to be 2.17, 2.73 and 2.76 for CHA-HT, CHA-Seed1 and CHA-Seed2, respectively (Table 1). An increase in the Si/Al ratio from CHA-HT to CHA-Seed1 was clearly observed, corresponding to the increase in signal intensity of Si(0Al) and Si(1Al). Also, it was found that these values were close to the ones obtained by EDS study (Table 1). However, a large difference was found between the Si/Al ratios determined by EDS and MAS NMR for CHA-Seed2, due to the presence of sanidine as evidenced by XRD.

Figure 4 shows the ^{27}Al MAS NMR spectra of CHA zeolites. The chemical shift of tetrahedrally coordinated Al atoms was found at 58.1, 58.6, 58.6 and 59.1 ppm for CHA-HT, CHA-Seed1, CHA-Seed2 and CHA-Seed3, respectively. The absence of the signals from octahedrally coordinated Al (around 0 ppm) suggests that Al atoms exist in the zeolite framework. The signal width became wider in CHA-Seed3 (9.108 ppm) as compared with CHA-HT (4.060), CHA-Seed1 (3.992) and CHA-Seed2 (4.449). Such broadening of resonance signals in CHA-Seed3 was consistent with the results of the ^{29}Si MAS NMR study.

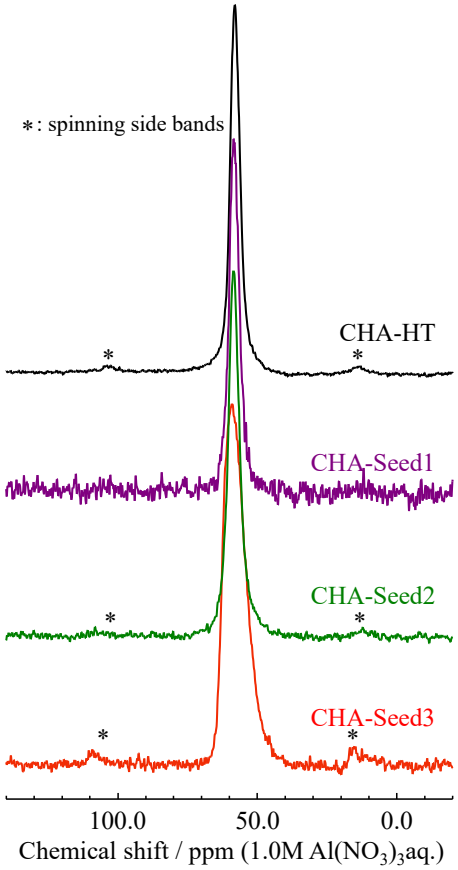

Fig. 4 ^{27}Al MAS NMR spectra of (a) CHA-HT, (b) CHA-Seed1, (c) CHA-Seed2 and (d) CHA-Seed3.

Finally, the N_2 adsorption isotherm of CHA zeolites at 77 K (Autosorb-1MP, Quantachrome Instruments, USA) were shown in Figure 5. The N_2 adsorption isotherm of CHA-HT did not indicate the occurrence of micropore filling (P/P_0 below 0.1), but showed a linear increase in N_2 adsorption up to about 0.8 (P/P_0) [13], suggesting the hindered access of N_2 molecules to micropores due to the presence of relatively large potassium cations (K^+). The K/Al ratio estimated by EDS was 1.1, 0.7 and 0.6 for CHA-HT, CHA-Seed1 and CHA-Seed2, respectively,

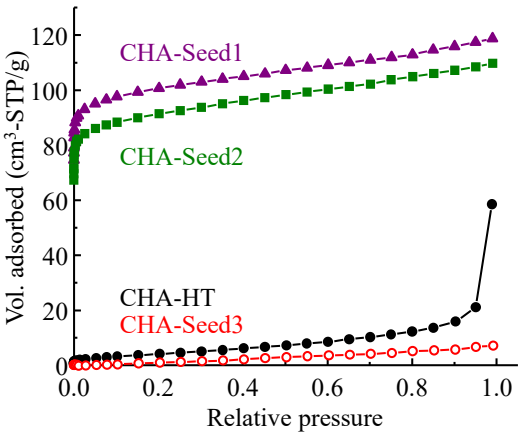

Fig. 5 Nitrogen adsorption isotherm of (a) CHA-HT, (b) CHA-Seed1, (c) CHA-Seed2 and (d) CHA-Seed3.

suggesting K^+ ions were filled almost fully in the cages of CHA-HT. As expected, CHA-Seed1 and CHA-Seed2 with lower K/Al ratios showed obvious micropore filling (type I by IUPAC classification) [18]. The N_2 sorption amount of CHA-Seed2 was slightly smaller than that of CHA-Seed1. This is due to the presence of non-porous sanidine in CHA-Seed2. For the mixture of sanidine and analcime (CHA-Seed3), the N_2 sorption amount was low in the whole (P/P_0) region. The BET (Brunauer-Emmett-Teller) surface area for CHA-HT, CHA-Seed1 and CHA-Seed2 was estimated to 14.0, 389.2 and 344.0 m^2/g, respectively. The surface area of CHA-Seed3 was lower than the value for detection limit (below 10 m^2/g).

In conclusion, CHA type zeolite was synthesized by seeded growth method, where OSDA-free CHA zeolite was used as seed crystals. The XRD measurements and ^{29}Si and ^{27}Al MAS NMR studies revealed that the obtained CHA zeolite were highly crystalized as compared with the initial material. However, the subsequent use of resultant CHA zeolite as seed crystals was found to be inappropriate, since other aluminosilicates – sanidine and analcime – were formed, resulting in a structure change.

References

[1] E. T. C. Vogt, G. T. Whiting, A. Dutta Chowdhury, B. M. Weckhuysen, Adv. Catal. 58 (2015) 143.
[2] http://www.iza-structure.org/databases/
[3] N. Nishiyama, M. Kawaguchi, Y. Hirota, D. Van Vu, Y. Egashira, K. Ueyama, Appl. Catal. A. Gen. 362 (2009) 193.
[4] X. Zhu, J. P. Hofmann, B. Mezari, N. Kosinov, L. Wu, Q. Qian, B. M. Weckhuysen, S. Asahina, JH. Ruz-Martínez, E. J. M. Hensen, ACS Catal. 6 (2016) 2163.
[5] Y. Ji, M. A. Deimund, Y. Bhawe and M. E. Davis, ACS Catal. 5 (2015) 4456.
[6] F. Gao, J. H. Kwak, J. Szanyi, C. H. F. Peden, Top. Catal. 56 (2013) 1441.
[7] R. Zhang, N. Liu, Z. Lei, B. Chen, Chem. Rev. 116 (2016) 3658.
[8] S. Vishnu Priya, T. Ohnishi, Y. Shimada, Y. Kubota, T. Masuda, Y. Nakasaka, M. Matsukata, K. Itabashi, T. Okubo, T. Sano, N. Tsunoji, T. Yokoi, M. Ogura, Bull. Chem. Soc. Jpn. 91 (2018) 355.
[9] S. I Zones, U.S. Patent 4,544,538, Oct. 1 (1985).
[10] S. I. Zones, J. Chem. Soc. Faraday Trans. 87 (1991) 3709.

[11] M. Bourgogne, J. L. Guth and R. Wey, U.S. Patent 4,503,024, March 5, 1985.
[12] M. Itakura, I. Goto, A. Takahashi, T. Fujitani, Y. Ide, M. Sadakane, T. Sano, Micropor. Mesopor. Mater. 144 (2011) 91.
[13] A. Taguchi, T. Nakamori, Y. Yoneyama, International Symposium on Zeolites and Microporous Crystals (ZMPC) 2018, Yokohama, submitted.
[14] H. Imai, N. Hayashida, T. Yokoi, T. Tatsumi, Micropor. Mesopor. Mater. 196 (2014) 341.
[15] Z. Liu, T. Wakihara, K. Oshima, D. Nishioka, Y. Hotta, S. P. Elangovan, Y. Yanaba, T. Yoshikawa, W. Chaikittisilp, T. Matsuo, T. Takewaki, T. Okubo, Angew. Chem. Int. Ed. 54 (2015) 5683.
[16] C. S. Cundy, P. A. Cox, Micropor. Mesopor. Mater. 82 (2005) 1.
[17] J. Klinowski, S. Ramdas, J. M. Thomas, C. A. Fyfe, J. S. Hartman, J. Chem. Soc. Faraday Trans. II, 78 (1982) 1025.
[18] M. Thommes, K. Kaneko, A. V. Neimark, J. P. Olivier, F. Rodriguez-Reinoso, J. Rouquerol, K. S. W. Sing, Pure Appl. Chem. 87 (2015) 1051.

富山大学水素同位体科学研究センター研究報告　第 37 巻

平成 30 年 7 月 20 日　発行
編集兼発行者
富山大学研究推進機構水素同位体科学研究センター
富山市五福３１９０

印刷所　前田印刷株式会社
富山市黒瀬 610－７
電話　076－407－1282

Published by Hydrogen Isotope Research Center, Organization for Promotion of Research,
University of Toyama
Gofuku 3190, Toyama 930-8555, Japan